

First black hole mass estimation for the quadruple lensed system WGD2038-4008

A. Melo¹, V. Motta¹, N. Godoy^{1,2}, J. Mejia-Restrepo³, Roberto J. Assef⁴, E. Mediavilla^{5,6}, E. Falco⁷, F. Ávila-Vera¹,
and R. Jerez¹

¹ Instituto de Física y Astronomía, Facultad de Ciencias, Universidad de Valparaíso, Av. Gran Bretaña 1111, Valparaíso, Chile.
e-mail: alejandra.melo@postgrado.uv.cl

² Núcleo Milenio de Formación Planetaria – NPF, Universidad de Valparaíso, Av. Gran Bretaña 1111, Valparaíso, Chile.

³ European Southern Observatory, Alonso de Córdova 3107, Vitacura, Santiago, Chile.

⁴ Núcleo de Astronomía de la Facultad de Ingeniería y Ciencias, Universidad Diego Portales, Av. Ejército Libertador 441, Santiago, 8320000, Chile.

⁵ Instituto de Astrofísica de Canarias, Vía Láctea S/N, La Laguna 38200, Tenerife, Spain.

⁶ Departamento de Astrofísica, Universidad de la Laguna, La Laguna 38200, Tenerife, Spain.

⁷ Harvard-Smithsonian Center for Astrophysics, 60 Garden St., Cambridge, MA 02138, USA.

September, 2021

ABSTRACT

Context. The quadruple lensed system WGD2038-4008 ($z_s = 0.777 \pm 0.001$) was recently discovered with the help of new techniques and observations. Even though black hole mass has been estimated for lensed quasars, it has been calculated mostly for one broad emission line of one image, but the images could be affected by microlensing, affecting the results.

Aims. We present black hole mass (M_{BH}) estimations for images A and B of WGD2038-4008 using the three most prominent broad emission lines ($H\alpha$, $H\beta$ and $MgII$) obtained in one single-epoch spectra. This is the first time the mass is estimated in a lensed quasar in two images, allowing us to disentangle the effects of microlensing. The high S/N of our spectra allows us to get reliable results and compare with the existing data in the literature.

Methods. We used the X-shooter instrument mounted in the Very Large Telescope (VLT) at Paranal Observatory, to observe this system taking advantage of its wide spectral range (UVB, VIS and NIR arm). The sky emission correction was made using Principal Component Analysis (PCA) as the nodding was small compared to the image separation. We compare the lines profiles to identify the microlensing in the broad line region (BLR) and corrected each spectra by the image magnification. Using the flux ratio between the continuum and the core of the emission lines we analyzed if microlensing was present in the continuum source.

Results. We obtained M_{BH} using the single-epoch method with the $H\alpha$ and $H\beta$ emission lines from the monochromatic luminosity and the velocity width. The luminosity at 3000 \AA was obtained using the Spectral Energy Distribution (SED) of image A while the luminosity at 5100 \AA was estimated directly from the spectra. The average M_{BH} between the images obtained was $\log_{10}(M_{BH}/M_{\odot}) = 8.27 \pm 1.05$, 8.25 ± 0.32 and 8.59 ± 0.35 for $MgII$, $H\beta$ and $H\alpha$ respectively. We find Eddington ratios similar to those measured in the literature for unlensed low-luminosity quasars. Microlensing of -0.16 ± 0.06 mag. in the continuum was found but the induced error in the M_{BH} is minor compared to the one associated to the macromodel magnification. We also obtained the accretion disk size using the M_{BH} for the three emission lines, obtaining an average value of $\log_{10}(r_s/cm) = 15.3 \pm 0.63$, which is in agreement with theoretical estimates.

Key words. gravitational lensing: macro – gravitational lensing: micro – quasar: individual: WGD2038 – 4008 – Black hole physics – quasars: supermassive black holes

1. Introduction

The number of lensed quasars discovered is consistently growing thanks to the help of new identification techniques and observations (Agnello et al. 2018; Krone-Martins et al. 2019; Lemon et al. 2020). Here, we study one of these recently identified lenses, WGD2038-4008. This system is a quadruple lensed quasar discovered in 2017 using a combination of Wide-field Infrared Survey Explorer (*WISE*, Wright et al. 2010) and *Gaia* (*Gaia* Collaboration et al. 2016) over the Dark Energy Survey (*DES*, Dark Energy Survey Collaboration et al. 2016) footprint with a source and deflector redshift of $z_s = 0.777 \pm 0.001$ and $z_l = 0.230 \pm 0.002$ respectively (Agnello et al. 2018). The deflector is a red galaxy with a compact bulge and a bright halo while the

source has an extended quasar host galaxy (Agnello et al. 2018). It has been observed using the Hubble Space Telescope (*HST*) obtaining a lens model for this system using LENSTRONOMY (Shajib et al. 2019). Spatially resolved narrow-line fluxes ([OIII] in Nierenberg et al. 2020) are also available. The lensing galaxy has been studied in Buckley-Geer et al. 2020 to measure its velocity dispersion and to identify the line-of-sight galaxies that need to be included in the lens model. Even though gravitational lensed quasars are a powerful tool to study the inner structure of active galactic nuclei (AGNs; Pooley et al. 2007; Anguita et al. 2008; Poindexter et al. 2008; Dai et al. 2010; Morgan et al. 2010; Treu 2010; Jiménez-Vicente et al. 2014; Motta et al. 2017), no such study has been conducted so far for WGD2038-4008. One of the difficulties of working with lensed quasars is that mi-

cro lensing could affect different regions of the broad emission lines (BELs) in the spectra of one (or more) image of the system (Mediavilla et al. 2011; Motta et al. 2012; Guerras et al. 2013; Fian et al. 2018; Rojas et al. 2020). Microlensing can affect the observed flux of the accretion disk and the BELs, as well as the shape of the BEL, ultimately adding uncertainty to the single-epoch black hole mass (M_{BH}) estimation.

Precise measurement of the M_{BH} is key in the understanding of the coevolution between the supermassive black hole (SMBH) growth and their host galaxy (see Ferrarese & Ford 2005; Kormendy & Ho 2013). In particular, physical parameters of the SMBH seem to correlate well with the luminosity (Marconi & Hunt 2003) and velocity dispersion (Ferrarese & Merritt 2000; Tremaine et al. 2002) of the host galaxy.

The single-epoch method (SE) is one of the most widely used technique to measure M_{BH} in AGNs, it relates the continuum luminosity of the quasar at a particular wavelength with the size of the broad line region (BLR) (see Vestergaard 2004; Shen & Liu 2012; Mejía-Restrepo et al. 2016). Typically, the SE masses for low redshift quasars ($z < 0.7$) are estimated in the optical using $H\alpha$ and $H\beta$ BELs and the continuum luminosity at 5100\AA . However, the Balmer lines are shifted into the infrared at higher redshifts, thus most of the estimations have been measured in the UV wavelength using MgII and CIV BELs. Over the last decade, SE method has been used to obtain M_{BH} in lensed AGNs (Peng et al. 2006; Greene et al. 2010; Assef et al. 2011; Sluse et al. 2012; Mediavilla et al. 2018), but most of them from the MgII and CIV BELs, and none of them using different emission lines observed simultaneously.

In this paper we present high signal-to-noise ratio (S/N) single-epoch spectra for the quadruple lensed system WGD2038-4008 to obtain the M_{BH} for three emission lines ($H\alpha$, $H\beta$ and MgII) for two of the images. We also study microlensing in the emission lines and in the continuum and finally we obtain the velocity dispersion of the lensing galaxy.

The paper is organized as follows. In Section 2 we present the data along with the reduction and the extraction of the spectra for each component. Section 3 shows the description of the method used for the estimation of the M_{BH} , microlensing analysis and velocity dispersion of the lensing galaxy. We present our results in Section 4 comparing with previous studies of different lensed quasars and finally our conclusions are presented in Section 5. We assume a Λ CDM cosmology with: $\Omega_\Lambda = 0.7$, $\Omega_M = 0.3$ and $H_0 = 70 \text{ km s}^{-1} \text{ Mpc}^{-1}$.

2. Observation and data reduction

2.1. Observational strategy

We obtained spectra for WGD2038-4008 during July of 2019 as part of ESO proposal ID 103.B – 0566(A) (PI: A. Melo) using the X-shooter instrument mounted at the 8.2 m UT2 at the Very Large Telescope (VLT), Paranal Observatory, Chile (Ver-net et al. 2011). X-shooter is a medium resolution spectrograph that observes in a wide spectral range, from ultraviolet (UVB; $3000\text{--}5600 \text{ \AA}$), through visible (VIS; $5500\text{--}10200 \text{ \AA}$) and up to the near-infrared (NIR; $10200\text{--}24800 \text{ \AA}$). We use three observing blocks (OBs) taken in two different nights with an average seeing of $1.12''$. The UVB slit was $1.0'' \times 11''$ (Spectral resolution $R = 5400$) while VIS and NIR slits were $1.2'' \times 11''$ ($R = 6500$ and 4300 for VIS and NIR) with a readout mode (UVB and VIS) of $100\text{k}/1\text{pt}/\text{hg}$ and a nodding of $3''$ per individual frame. Each UVB/VIS (NIR) OB consist of 2 (4) exposure frames. The atmospheric dispersion corrector (ADC)

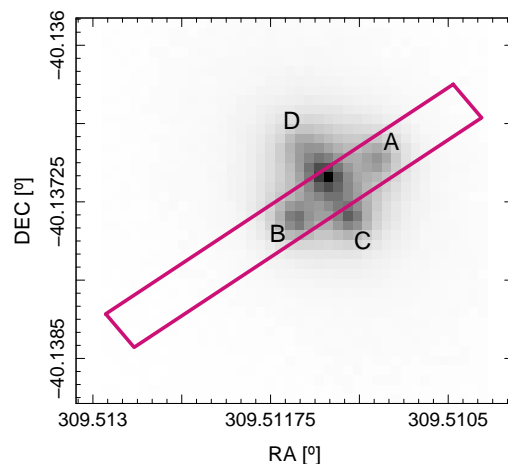


Fig. 1. Scheme of the slit position centered on image B (RA 307.5115875 , DEC -40.13736167 , epoch J2000) of WGD2038 – 4008. The FITS image is from the Dark Energy Survey (DES) in filter r^1 .

is used to avoid chromatic differential atmospheric refraction. Table 1 summarizes the main observational characteristics of WGD2038 – 4008.

The slit position was chosen to cover the two brightest source images, centered in image B of the gravitational lensed quasar with a position angle on the sky of 126.8514° to include image A (see Figure 1).

2.2. Data processing

We used the ESO pipeline *EsoReflex* (Freudling et al. 2013) workflow with the X-shooter pipeline version 3.5.0 to reduce each OB without using nodding to subtract the sky emission. This method was employed instead of the standard one because the $3''$ nodding is comparable to the image separation ($\sim 2.87''$), causing a self-subtraction flux from the lensed quasar spectra. The next steps in the reduction and extraction were slightly different for the three arms of the instrument. Once the frames were corrected by cosmetics (flat field, dark current, wavelength calibration, among others), we proceeded to subtract the sky emission in the NIR arm. We designed a sky emission correction for each individual frame based on Principal Component Analysis (PCA, Deeming 1964; Bujarrabal et al. 1981; Francis & Wills 1999), a method normally used in multi-dimensional analysis. PCA uses a basis of eigenvectors that are constructed to describe the data (by maximizing the variance of the projected data, for instance). This method is usually applied to reduce the number of parameters describing a data set by computing the principal components to change the representation of the data. The number of components used in the reconstruction was chosen to minimize the standard deviation of the residuals between the spectrum and all sky models (using different number of components). The procedure to obtain the best representation of the underlying sky emission in each frame had the following steps. First, the outliers (such as bad pixels) were masked using σ -clipping ($\sigma=5$

¹ Gravitational Lensed Quasar Database <https://research.ast.cam.ac.uk/lensedquasars/>

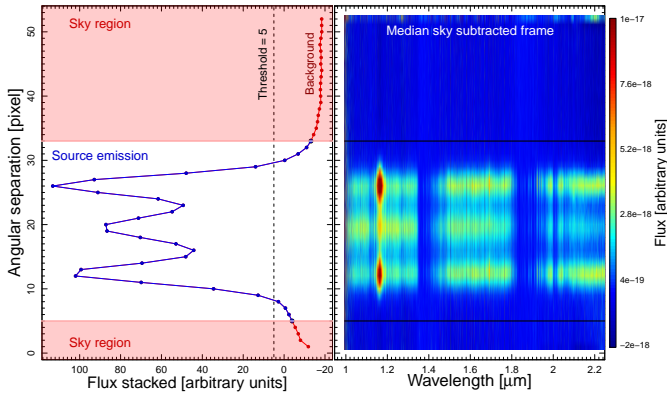


Fig. 2. *Left:* Collapsed frame along the wavelength axis after the subtraction of the sky median. The pink shaded zone represent the sky region (see text below). *Right:* NIR frame after sky subtraction.

with three iterations), replacing them with an estimated value obtained from a bicubic interpolation using the surrounding pixels. Then, we calculated the median for each wavelength bin to obtain a rough approximation of the sky emission as a function of the wavelength. Note that this value will only be used to identify the targeted spectra (quasar lensed images A and B, as well as the lens galaxy). We subtract this rough sky median from each frame and collapse the remaining 2D spectra along the wavelength (see Figure 2 right and left, respectively) to select an uncontaminated spatial region for the sky emission. A threshold equal to 3 pixels (above and below) the dispersion of the median above the background (see Figure 2, left) is applied to choose the region that is going to be employed as the PCA-basis (normalized to the unit). The PCA eigenvector basis is obtained by constructing a model of the sky emission in the selected spatial region, this 2D sky model is then subtracted from the frame.

Flux calibration is done by using the response curve from the end-products of the X-shooter pipeline. This response is obtained from a standard star observed the same night as the target, in our case GD153, EG 274 and Feige 110 for OB 1, 2 and 3, respectively.

After the sky modelling and subtraction, we employ `molecfit` (Smette et al. 2015; Kausch et al. 2015) in each frame to correct by telluric absorptions. For each frame, the target spectra were median-combined into a single spectrum in order to increase the signal and decrease the noise. The spatial region occupied by the targets was previously calculated during the PCA sky emission estimation, and corresponds to the source emission region in Figure 2. The `molecfit` best-fit was applied to each frame row-by-row. Once the frames are corrected by sky emission and telluric absorption, they are median combined and the uncertainties are estimated as the median absolute deviation. All the parameters required for the stacking (dithering, pixel scale, among others) were obtained from the header of each frame, modified by the X-shooter workflow. Figure 3 shows the result of the final 2D spectrum (top panel) compared to the one obtained as end-product from the ESO pipeline (bottom panel).

In contrast to the NIR, the VIS observations are not dominated by the sky brightness. Therefore, instead of the PCA analysis, we use the median of each sky region as the best representation of the sky brightness, obtained in the same way as for the NIR (selecting a region free of source emission to compute the sky brightness representation). The flux calibration, telluric correction, and combination of frames are done in the same way

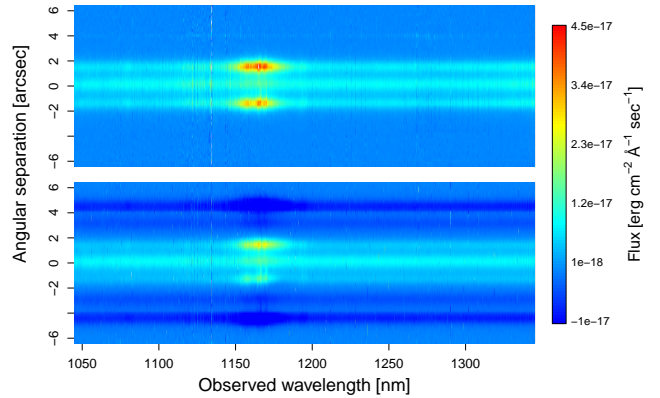


Fig. 3. Final 2D NIR spectrum using PCA sky extraction described in Section 2.2 (Top Figure) compared to the one using ESO pipeline reduction (bottom figure). Both spectra are flux calibrated and telluric corrected.

as for the NIR arm. Even though the UVB arm does not require sky subtraction, we use the same procedure as the VIS arm to be consistent with the reduction.

2.3. 1D extraction

Due to the small separation between the quasar images A, B and the lens galaxy, there can be cross-contamination in their spectra (see Fig. 1). To obtain uncontaminated spectra we proceed as follows. First, we collapsed the 2D reduced spectrum along the wavelength axis in a high S/N region, for example around an emission line region ($H\alpha$ in the NIR, OIII in VIS and MgII in the UVB arm). In the case of the VIS and UVB arms, we selected bins of 20 pixels (4 \AA) to increase the signal-to-noise of the sources. We masked the outliers (persistent bad pixels, poor sky subtraction and/or low signal to noise regions) to obtain the best fit parameters as a function of the wavelength. The spatial contribution of each component is estimated by simultaneously fitting three Gaussian profiles. The distances between image A and B ($\sim 2.87 \text{ arcsec} \approx 14 \text{ pixels}$), and between image A and the lens galaxy projection onto the AB segment ($\sim 1.47 \text{ arcsec} \approx 8 \text{ pixels}$) are used to fix the position of the Gaussian centers for B and the lens galaxy, respectively. Assuming A and B are point sources, we can consider that they have the same FWHM (and standard deviation parameter - σ), and a variable σ_l (larger than σ , due its extended emission) for the lensing galaxy in UVB and VIS arms. Due to the faintness of the lens galaxy in the NIR arm, the σ_l value of the lens galaxy is considered the same as for the images ($\sigma_l = \sigma$). Thus, the free parameters are the amplitudes, image A center, σ for the point sources (and lens galaxy in NIR) and σ_l for the lens galaxy (in the UVB, VIS arms). Using the best-fit estimated values and their respective uncertainties, we construct a probability function for the spatial distribution of each target (quasar images and lens galaxy), allowing to identify the probability that a given spatial pixel belongs to one of the targets. We use error propagation for each free parameter to estimate the related uncertainties in each final, uncontaminated spectra.

Considering the seeing variation along the wavelength range and the selected slit width, we need to estimate the percentage of lost flux. We estimated the broadening of the spectra profile due to the instrumental dispersion at different wavelengths by fitting a

Gaussian function for each wavelength bin of the telluric standard star (HD 115470 for the case of OB 1 of seeing $0.75''$). The σ_{\odot} obtained was of $0.76''$ with a dispersion that does not vary from 1 pixel between the arms. We use this value (see in Table 1) to calculate the percentage of flux entering the slit by simulating the system as a sum of Gaussian functions and sigma obtained from the header and integrating it within the slit using the seeing delivered in the header. The percentage of flux lost was 30.5% in UVB, 14.9% in VIS and 19.74% in NIR. These values will be included as an extra flux error in all our analysis.

After extracting the spectra for the three components, we notice that the lens galaxy spectrum shows contamination by quasar emission lines. Given the amount of contamination, the slit width and position angle, we infer this is a contribution from image C (see Fig. 1). To obtain the uncontaminated lens galaxy spectrum, we use spectrum A as a proxy for C and estimate the C contribution fraction for each arm (0.25 for NIR, 0.43 for VIS and 0.5 for UVB arm) that removes the quasar emission lines. The S/N of the emission line and continuum were obtained by estimating the standard deviation of the background. We use the 2D spectra to obtain the background emission (sky emission in Section 2.2), getting the mean and standard deviation of this background. We then choose a continuum region located around the emission line (50 \AA) for each signal contribution (image A, B and the lensing galaxy) and obtain the mean value. With these values we calculate the S/N of the continuum. We calculate the S/N of the emission lines using the same method, i.e. selecting the same spatial region but estimating the mean in a reduced wavelength window (approximately 300 to 500 \AA) around each emission line. The S/N for each continuum and emission line are listed in Table 2. The final spectra for images A, B and the lensing galaxy (uncontaminated by the quasar emission) is presented in Fig. 4. As the ADC did not work during the night that OB 1 and 2 were taken, the UVB and VIS arm experienced flux loss (Fig. 4), explaining the atypical profile of the AGN spectra (see Vanden Berk et al. 2001 and Glikman et al. 2006 for a composite quasar spectra). This loss will affect the luminosity measurement, specially in the UVB arm (See section 3.1 for more details).

3. Methods

Black hole mass is estimated by using the single-epoch method (SE method; e.g. McLure & Dunlop 2004; Shen et al. 2008; Trakhtenbrot & Netzer 2012), which combines the usage of the Doppler line width of the broad emission line and the monochromatic luminosity to obtain a proxy for M_{BH} . If we assume that the emitting gas in the BLR is virialized:

$$M_{BH} = f R_{BLR} (\Delta v)^2 G^{-1}, \quad (1)$$

where G is the gravitational constant, R_{BLR} is the BLR size, $(\Delta v)^2$ is the velocity of the line emitting gas in the BLR, and f is the virial factor that depends on the unknown structure, kinematics, inclination and distribution of the BLR (Peterson et al. 2004 and references therein). The BLR size comes from the Reverberation Mapping (RM, Blandford & McKee 1982; Peterson 1993) and with the known correlation between the AGN luminosity and the size of the BEL, $R_{BLR} \sim (\lambda L_{\lambda})^{\alpha}$ (e.g. Kaspi et al. 2000, 2005; Bentz et al. 2009), allowing us to estimate M_{BH} as:

$$\log(M_{BH}) = \log(K) + \alpha \log\left(\frac{\lambda L_{\lambda}}{10^{44} \text{ erg/s}}\right) + 2.0 \log\left(\frac{FWHM}{1000 \text{ km/s}}\right), \quad (2)$$

where $K = G^{-1} f$. Although, the literature shows different values for the parameters K and α (McLure & Dunlop 2004; Vestergaard & Peterson 2006; Vestergaard & Osmer 2009; Shen et al. 2011), we use those estimated by Mejía-Restrepo et al. 2016 because they were estimated using a similar observing setup, thus minimizing the systematic effects. In particular, the sample of Mejía-Restrepo et al. 2016 not only contains several emission lines for each object but also all lines for a single object were observed simultaneously. The values for the parameters used for the emission lines ($H\alpha$, $H\beta$ and $MgII$) at their respective luminosities (L_{5100} , L_{5100} , L_{3000}) are:

$$\begin{aligned} (\log K, \alpha)_{H\alpha} &= (6.845, 0.650) \\ (\log K, \alpha)_{H\beta} &= (6.740, 0.650) \\ (\log K, \alpha)_{MgII} &= (6.925, 0.609) \end{aligned}$$

Besides the usual uncertainties related to the SE method (FWHM, luminosity, and f parameter estimations), the observed source luminosity needs to be corrected for the lensing magnification. To obtain the magnification factor (μ) we use the convergence (κ) and shear (γ) parameters estimated from the lens model as $\mu = 1/[(1 - \kappa)^2 - \gamma^2]$ (Narayan & Bartelmann 1996). Employing the values previously calculated by Shajib et al. 2019, we obtain a magnification factor of $\mu_A = 2.27 \pm 0.21$ and $\mu_B = 2.71 \pm 0.32$.

3.1. Emission line fitting and luminosity measurement

After demagnifying the spectra, and removing the continuum and the iron template, (following Mejía-Restrepo et al. 2016), we model each emission line profile and estimate the BEL FWHM. We used Gaussian functions to represent the broad and narrow components of each emission line (see Table 4 of Shang et al. 2007) and mask those regions affected by absorptions². In the $H\alpha$ region we added four extra Gaussian components for [N II] and [S II] NLR doublets. In the $H\beta$ region we considered two extra Gaussians for the [O III] NLR doublet and one for the He II broad emission line. For the Mg II region we considered two narrow and broad Gaussian components. The FWHM used for the M_{BH} measurement is obtained from the standard deviation of line profile after removing the NLR component (i.e. the resulting profile is the combined Gaussians representing the broad line components). The uncertainties were obtained using error propagation and a Monte-Carlo simulation of 1000 random resamplings, assuming a Gaussian distribution for the flux uncertainty at each pixel. The best line fit is shown in red in Figure 5. As every emission line exhibits some kind of distortion (possible absorptions) that could lead to an overestimation of their FWHM, we decided to mask those regions for the Gaussian fitting. Mg II profile has several absorption features (masked region [2787:2794, 2796:2802] \AA), possible caused by the circumgalactic medium (CGM). In the case of $H\alpha$, the feature perceived as absorption masked region [6525:6547, 6569:6576] \AA could be instead a very bright NLR. Similarly, $H\beta$ shows a distorted profile (masked region [4835:4849, 4866:4878] \AA) possibly related to a poor FeII fitting. Monochromatic luminosity was measured using continuum windows on each side of the emission line ([4670 : 4730, 5080 : 5120] \AA for $H\beta$ and [6150 : 6250,

² We should point out that we also considered other line profile fittings: i) Gaussian fitting without masking regions, ii) the addition of Gaussian profiles for the absorption features. Although both methods provide FWHM that are consistent with our results, the first one yields larger residuals and the last one introduces overfitting.

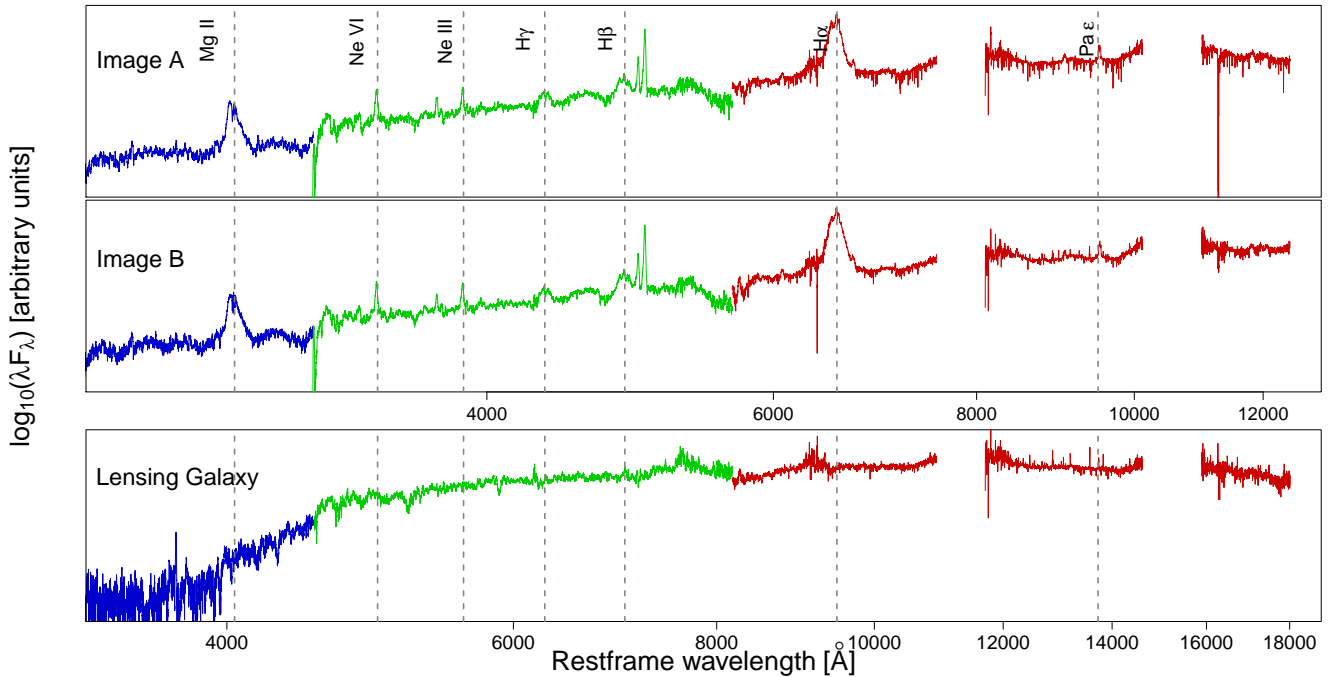


Fig. 4. Rest-frame X-Shooter spectra for image A, image B and the lensing galaxy. Colors represent the different arms of the instrument: UVB (green), VIS (blue) and NIR (red). The images are corrected by their respective redshift ($z_s = 0.777$ and $z_l = 0.230$). The atmospheric windows are left blank for the NIR band. The lensing galaxy is uncontaminated by the quasar emission. The wavelength is in the rest frame of the respective object and the position of the emission lines are shown as dashed lines.

Table 1. Log of the observation for the three OBs.

OB	Date	Arm	Exp. time (seconds)	Number of Exposures	Airmass	Seeing ⁽¹⁾ (")
1	9/10 July 2019	UVB	600	2	1.067	1.02
		VIS	600	2	1.068	1.09
		NIR	600	4	1.065	1.08
2	9/10 July 2019	UVB	600	2	1.133	1.08
		VIS	600	2	1.134	1.02
		NIR	600	4	1.127	1.01
3	10/11 July 2019	UVB	600	2	1.133	1.27
		VIS	600	2	1.134	1.30
		NIR	600	4	1.127	1.28

Notes. ⁽¹⁾ This seeing corresponds to the delivered seeing on Image Analysis detector given in the header of each frame.

6800 : 6900] Å for $H\alpha$). These spectral windows have been selected due to the small (or even null) emission line contamination, and were used to interpolate the region of interest following a single power-law function. As mentioned before, the flux loss in the UVB and VIS arms impede the use of the spectra to estimate the monochromatic luminosity at 3000 Å. Instead, we estimated this luminosity by fitting a Spectral Energy Distribution (SED; template of Assef et al. 2010) to the unmagnified magnitudes obtained from HST (Shajib et al. 2019) and DES (Agnello et al. 2018). Compared to the luminosity measurement, the FWHM of $MgII$ FWHM is not affected by this flux loss.

The FWHM obtained from the line profile fitting and the monochromatic luminosity (estimated from the continuum and SED) for each emission line in image A and B is presented in Table 2.

3.2. Microlensing analysis

Microlensing can induce flux variations in the quasar images due to lensing from stars in the lensed galaxy halo (see for instance Chang & Refsdal 1979; Wambsganss 2006). This flux variation in one (or more) images is sensitive to the angular size of the source, meaning that the magnification will be bigger for a smaller emitting region. Given the latter, we could study the inner structure of WGD2038-4008 from the single-epoch images of different observations, where the accretion disk and BLR can be affected differently by microlensing and could affect the wings of the emission lines. On the contrary, the Narrow Line Region (NLR) is insensitive to microlensing and can be used as the baseline (Abajas et al. 2002). To investigate whether microlensing is present, we use the magnitude difference between the emission line core and the continuum (see Moustakas & Metcalf 2003; Mediavilla et al. 2009, 2011; Motta et al. 2012; Guerras et al. 2013; Motta et al. 2017; Rojas et al. 2020). The quasar emission lines have different components, meaning that

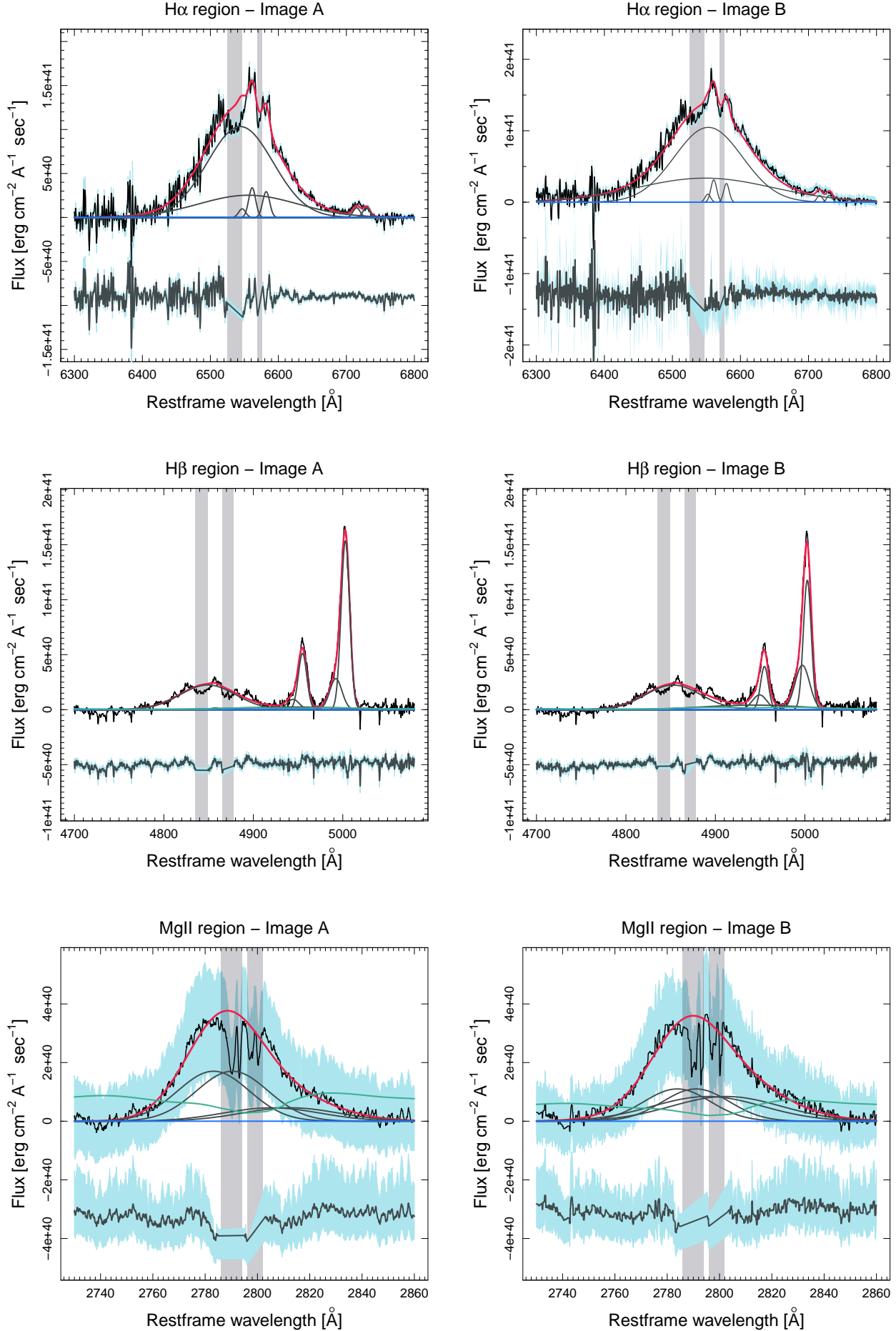


Fig. 5. Gaussian fitting of H α , H β and MgII regions for images A (left) and B (right). Red line represents the best fit, black lines represent the different components of each region (emission and absorption), green line represents the Fe template and the blue line is the continuum fit of the spectra. 1-sigma error of the spectra along with the residuals and their respective errors are in the bottom of the images.

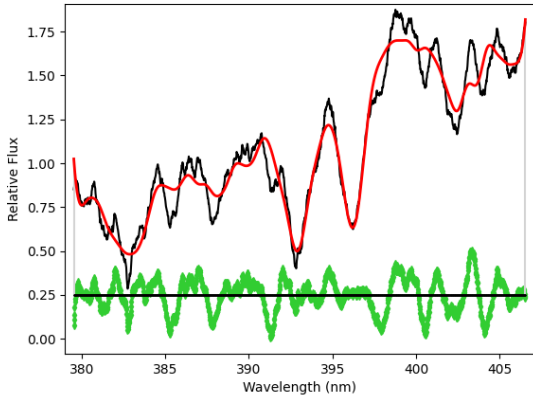


Fig. 6. Fit of stellar templates to the lensing galaxy using pPXF package after removing the extra quasar contribution.

they come from different inner regions of the AGN, the line core will be dominated by the NLR while the wings are dominated by the BLR emission. Also, the light of each image follows a different path through the lens galaxy where gas and dust can produce extinction. We can separate microlensing from extinction considering that only the latter will affect both the continuum flux ratio and the core of the emission line (Falco et al. 1999; Motta et al. 2002; Mediavilla et al. 2005). We obtain the magnitude difference between components in the continuum by fitting a straight line between two regions in each side of each emission line. The regions have a size of $\sim 30\text{--}40\text{\AA}$. We integrated the line between the two regions to obtain the continuum flux for both images. This continuum is then subtracted from the spectrum and we integrate a small window (between $10\text{--}30\text{\AA}$) centered in the emission line core to obtain the flux uncontaminated by the continuum. Integrating in the core of the emission line decreases the BEL contamination that can also be affected by microlensing. The uncertainty of the flux is assumed to be related to the continuum fitting and is obtained using error propagation, where the square root of the error in the spectra and the straight line are added in quadrature. Finally, the magnitude difference between image A and B for each region (continua and line cores) is $m_A - m_B = -2.5 \log(F_A/F_B)$, obtaining a $(m_A - m_B)^{\text{line}}$ for the core of the emission line and a $(m_A - m_B)^{\text{cont}}$ for the continuum.

3.3. Stellar velocity dispersion of the lens galaxy

The stellar velocity dispersion (σ) of a galaxy measures the random motion of stars due to a presence of a mass. Obtaining an accurate value of σ is important to restrict the lens model parameters, and together with the light curves of the images of the lensed quasar measure the Hubble Constant H_0 and helps to improve the uncertainties. The velocity dispersion was estimated from the lens galaxy spectrum using the Penalized Pixel-Fitting (pPXF; Cappellari & Emsellem 2004; Cappellari 2017). We use the rest-frame wavelength 3600 to 4200\AA for the UVB arm and 4800 to 5800\AA for VIS arm. The spectra was fitted using the Single Stellar Population library by Vazdekis et al. 2010 included in pPXF (see Figure 6). The velocity dispersion obtained was 299 ± 12 km/s, consistent with the measurements of Buckley-Geer et al. 2020 (296 ± 19 km/s and 303 ± 24 km/s using Gemini South/GMOS-S spectra).

4. Results

We identified the three most prominent emission lines of the lensed quasar (MgII, H β and H α) with high S/N (see Table 2). The spectra were de-magnified using the parameters from the lens model of Shajib et al. 2019 and the continuum was subtracted to compare the profiles of image A and B (Fig. 7). Interestingly, we find an enhancement of the right wing of H α emission line of image B compared to image A (between ~ 6600 and 6700\AA). This magnitude difference ($\sim 0.28 \pm 0.03$ mag integrated in the region $[6591.4:6686.5]\text{\AA}$) could be explained assuming that microlensing is affecting the H α broad emission line. This effect should also be seen in the H β profile as it arise from a similar region size as H α . However, we do not detect this effect, although this could be due to the low S/N of H β ($S/N \lesssim 20$) compared to H α ($S/N \gtrsim 72$) and to the presence of absorption-like features. There is no sign of such effect in the MgII profile ($S/N \lesssim 31$), which is reasonable because MgII emission is produced in a farther away region than the Balmer lines (Goad et al. 2012) and hence is less susceptible to microlensing effects.

Multi Gaussian fitting of image A and B are shown in Figure 5 following the procedure described in Section 3.1. The grey shaded regions represent the masked sections used during the fitting. Table 2 shows the FWHM estimated for each broad emission line in each quasar image. Even though the components of MgII have a slight different amplitudes due to the absorption that are contributing to the profile, the FWHM values are within the errors. The FWHM of H β are in good agreement in spite of the low S/N. In the case of H α , the estimated FWHM are different (>5 sigma) and we will discuss below how this might affect our M_{BH} estimations. To investigate whether microlensing is present in the continuum, we obtained the magnitude difference between the core of each emission line uncontaminated by the continuum, $(m_A - m_B)^{\text{line}}$, and the continuum under the emission line, $(m_A - m_B)^{\text{cont}}$, shown in Fig. 8. The H α emission line region shows two values corresponding to two emission line peaks, avoiding the right wing (see Figure 7), integrated in the windows $[6500.1:6526.0, 6547.7:6565.4]\text{\AA}$, respectively. The H β region shows three values corresponding to H β ($[4820:4890]\text{\AA}$ integration window) and the [OIII] doublet emission line cores ($[4949.2:4960.0, 4996.4:5007.0]\text{\AA}$ integration window). We included the MgII region integrated between $[2774.6:2784.1]\text{\AA}$ and Paschen ϵ $[9512.0:9533.0]\text{\AA}$. Considering that the magnitude difference in the emission lines is approximately constant, we use the median and its standard error, $(m_A - m_B)^{\text{line}} = 0.17 \pm 0.05$ mag, as our baseline of non-microlensing. As the values for the integrated continuum also yield a roughly constant value along the wavelength, we use the median to estimate $(m_A - m_B)^{\text{cont}} = 0.01 \pm 0.03$ mag. We compare our result with spectroscopic data of the integrated flux obtained by Nierenberg et al. 2020 (see Fig. 8) $(m_A - m_B)^{\text{cont}} = -0.06 \pm 0.09$ and $(m_A - m_B)^{\text{line}} = 0.16 \pm 0.02$, which is in agreement with our magnitude difference for the continuum and emission line in the H β region, respectively. Published data from broadband photometry (Agnello et al. 2018; Lee 2019; Shajib et al. 2019 taken between 2016 and 2017) is also included in the Fig. 8. We fit a median function to these values obtaining $(m_A - m_B)^{\text{lit}} = 0.21 \pm 0.06$ mag. The values are in agreement with the core of our narrow emission lines.

Since the above mentioned data are not time-delay corrected, the magnitude difference estimated from our spectra, $\Delta m = (m_A - m_B)^{\text{cont}} - (m_A - m_B)^{\text{line}} = -0.16 \pm 0.06$ mag., could

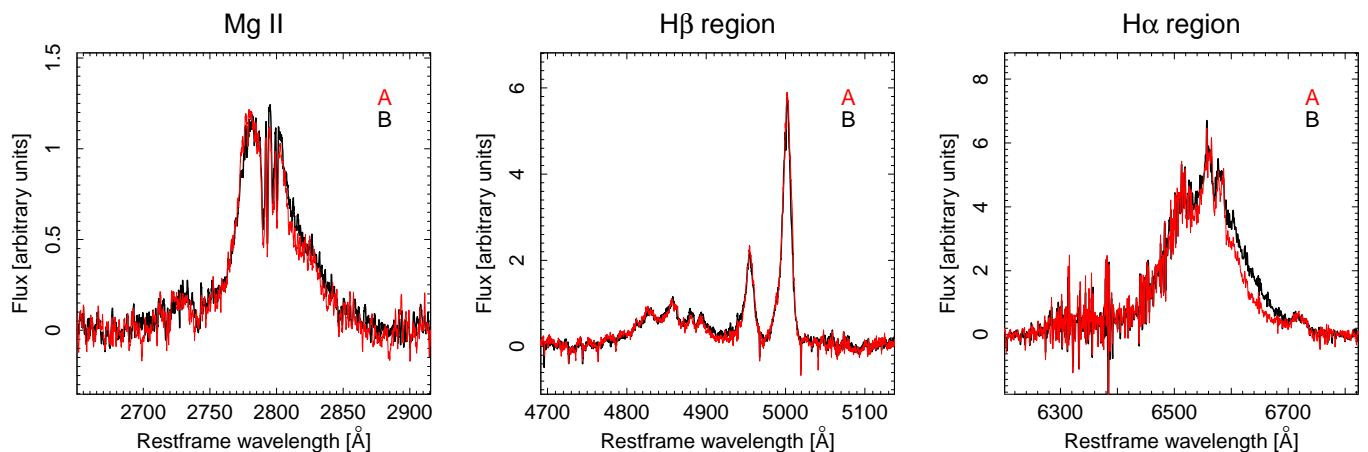


Fig. 7. MgII, H β and H α emission line region. The images are demagnified using the magnification values given in section 3.

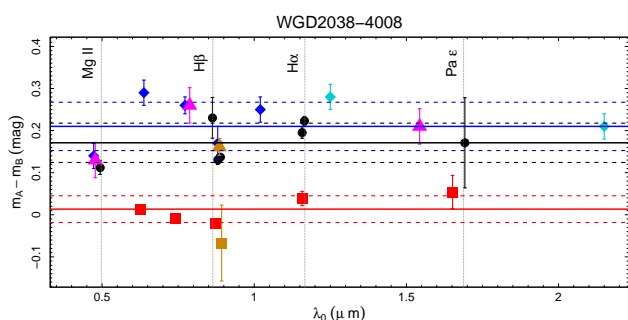


Fig. 8. Magnitude difference $m_A - m_B$ vs λ_0 between images A and B. Red squares shows the integrated continuum and in black circles the emission line core without the continuum using X-shooter. We include measurements obtained from the literature: HST Shajib et al. 2019 (magenta triangles), VISTA Lee 2019 (cyan diamond), DES Agnello et al. 2018 (blue diamond) and HST F105W/G102 Nierenberg et al. 2020 (orange square for continuum and orange triangle for a narrow emission line). The Red line is the median of the continuum and the dotted red line the standard deviation, the black line for the emission line core and the blue line for the literature.

be due to intrinsic variability coupled with a time lag between the images. We use the Yonehara et al. 2008 procedure to estimate such effect. We assume the structure function inferred from imaging data of quasars (Vanden Berk et al. 2004), an absolute magnitude range for the source in I band, $M_I = (-21, -30)$, the predicted time delay for the quasar images $\Delta t_{AB} = -6 \pm 1$ days (Shajib et al. 2019), and assume no lag between our observations as they were obtained with 1 day of difference. We obtained a magnitude difference induced by time delay coupled with intrinsic variability of 0.05 mag (0.03 mag) to 0.07 mag (0.04 mag) for a -21. mag (-30. mag) source in the F160W and F475W HST broad-band filters, respectively. On the other hand, we also use light-curves obtained by COSMOGRAIL (e.g. Bonvin et al. 2017; Courbin et al. 2011; Eigenbrod et al. 2005), which has a monitoring program to obtain time delay between multiple images of lensed quasars. WGD2038-4008 follow-up is carried out in MPIA 2.2m telescope (La Silla Observatory, Chile) with an average of one measurement per week (F. Courbin private communication), although no time delay has been measured yet. We considered three dates that were 7 days apart and within 2 weeks of our X-shooter observations, then shift the B data to correct by time delay, and estimate the average magnitude difference as

$(m_A - m_B)_{corr} \sim 0.16 \pm 0.03$. This value is in good agreement with our estimation using the core of the emission lines. Therefore, $\Delta m = -0.16 \pm 0.06$ mag seems to indicate the presence of constant/or long-lasting microlensing event not detected by the light curves (Sluse & Tewes 2014). To investigate this possibility, we estimate the time scale associated to such event. Following Treyer & Wambsganss 2004, we define two time scales: 1) the standard lensing time (t_E), and 2) the crossing time (t_{cross}). The first one represents the time it takes a star to cross a length equivalent to the Einstein radius:

$$t_E = (1 + z_L)R_E/v_{\perp} \quad (3)$$

where z_L is the lens redshift, R_E the Einstein radius in the source plane and v_{\perp} the effective source velocity (Treyer & Wambsganss 2004). The second time scale, refers to the time that, within the length of an Einstein radius, the source may encounter a caustic line, causing a large magnification:

$$t_{cross} = (1 + z_L)R_{source}/(v_{\perp}(D_S/D_L)) \quad (4)$$

where R_{source} is the quasar size (i.e. the accretion disc size, $\log_{10}(r_s/\text{cm}) = 15.65$), and D_S and D_L the angular diameter distance (Hogg 1999) of the observer-source and observer-lens respectively with our assumed cosmology. Considering a typical value of $v_{\perp} = 600 \text{ km s}^{-1}$ as assumed by Treyer & Wambsganss 2004, we estimate $t_E \simeq 27.7$ years and $t_{cross} \simeq 0.6$ year. On the other hand, if we calculate the effective source velocity following Mosquera & Kochanek 2011³, we obtain $v_{eff} = 820 \text{ km s}^{-1}$, which yields $t_E \sim 20.3$ years and $t_{cross} \simeq 0.5$ year, respectively. Thus, a long-lasting microlensing event would last for ~ 20 years, while the crossing time should be around 6 months.

In spite of this microlensing magnification, the induced error in the luminosity is negligible as the majority of the error budget is introduced by the macro model magnification (Sec.3).

The monochromatic luminosity at L_{5100} was estimated using a single-power law function between two continuum windows on each side of the BELs. It agrees for H α and H β of each image, within the errors, with an average value of $\log_{10}(L_{5100}/L_{\odot}) = 44.29 \pm 0.03$. Due to flux loss in UVB, we modeled a SED to estimate L_{3000} using the magnitudes and magnification of image A, obtaining $\log_{10}(L_{3000}/L_{\odot}) = 44.23 \pm 0.19$. The luminosities L_{300} and L_{5100} agree within their errors, even though they

³ Notice that in Mosquera & Kochanek 2011 these time scales are defined as $t_{cross} = R_{source}/v_{eff}$ and $t_E = R_E/v_{eff}$, where v_{eff} is the effective velocity and is defined as a combination of the motions of the observer, the lens, and the source.

were obtained with different methods. The M_{BH} was obtained following eq. 2 with an average value between A and B images of $\log_{10}(M_{BH}/M_{\odot}) = 8.59 \pm 0.35, 8.25 \pm 0.32, 8.27 \pm 1.06$ for $H\alpha$, $H\beta$ and $MgII$, respectively. The M_{BH} estimates obtained using the three different emission lines are consistent within 2 sigma. We show the M_{BH} estimations along with those of the literature of lensed quasars in Figure 9. To avoid the discrepancies associated to the different parameter values used by the authors, we combine their FWHM and monochromatic luminosity values using equation 2 to obtain M_{BH} . We converted from intrinsic to bolometric luminosity applying $L_{bol} = A L_{ref}$, where $A = (3.81, 5.15, 9.6)$ for $L_{ref} = (L_{1350}, L_{3000}, L_{5100})$ presented in Sluse et al. 2012. M_{BH} estimates for 33 lensed quasars are also included in Fig. 9 (some of them having several values as they are obtained from different emission lines) as well as those of Shen et al. 2019 for (non-lensed) quasars from SDSS reverberation mapping. The Figure shows that our results for image A and B of WGD2038-4008 are in good agreement with those of the non-lensed quasars, situating our object in the low luminosity range of the diagram.

We can also infer the accretion disk size (r_s) assuming a thin-disk model (Shakura & Sunyaev 1973) and considering our M_{BH} estimate (Mosquera & Kochanek 2011) as:

$$r_s = 9.7 \times 10^{15} \left(\frac{\lambda_{rest}}{\mu m} \right)^{4/3} \left(\frac{M_{BH}}{10^9 M_{\odot}} \right)^{2/3} \left(\frac{L}{\eta L_E} \right)^{1/3} \text{ [cm]} \quad (5)$$

λ_{rest} is the wavelength where the M_{BH} is measured, η is the accretion efficiency and L/L_E the luminosity in units of the Eddington luminosity. For a typical accretion rate $\eta = 0.1$ and $L/L_E \sim 1/3$ (Schulze & Wisotzki 2010). Using the different M_{BH} estimates with the wavelength value at $H\alpha$, $H\beta$ and $MgII$, the accretion disk size measurements are shown in Table 2. The size $MgII$ has an average of $\log_{10}(r_s/\text{cm}) = 14.98 \pm 0.84$, $H\beta$ is 15.25 ± 0.4 and $H\alpha$ 15.67 ± 0.74 . Our estimates are in agreement within each other and with Morgan et al. 2018. We scaled our wavelength (λ in which the M_{BH} was measured) to 2500 \AA , assuming $r_s \propto \lambda^{4/3}$ and obtained $\log_{10}(r_s/\text{cm}) = 14.94 \pm 0.22, 15.25 \pm 0.82$ and 15.65 ± 0.79 in $MgII$, $H\beta$ and $H\alpha$ respectively. These values are consistent with the theoretical values estimated by Morgan et al. 2018 at r_{2500} : 15.41 ± 0.15 for $MgII$, 15.37 ± 0.26 for $H\beta$ and 15.62 ± 0.18 for $H\alpha$.

5. Conclusions

We have obtained high S/N observations for the quadruple lensed system WGD2038-4008 using X-shooter instrument in VLT. We use Gaussian fitting to obtain uncontaminated spectra for the A and B lensed quasar images and the lens galaxy. The most prominent emission lines are detected ($MgII$, $H\beta$ and $H\alpha$) as well as absorption lines in the lensing galaxy.

We confirmed the velocity dispersion of the lensing galaxy spectra, obtaining $299 \pm 12 \text{ km/s}$, in agreement with previously estimated values ($2.96 \pm 19 \text{ km/s}$ Buckley-Geer et al. 2020).

The magnification factors were estimated from the lens parameters of Shajib et al. 2019 ($\mu_A = 2.27 \pm 0.21$ and $\mu_B = 2.71 \pm 0.32$) and were used to demagnify the spectra. Comparing the continuum-subtracted emission lines, we notice there is an enhancement in the right wing of $H\alpha$ of image B, that could be due to microlensing. However, this effect is not seen in $H\beta$ (a region similar in size to $H\alpha$) but this might be because of the low S/N and to the presence of absorption-like features. $MgII$ profile does not show any sign of microlensing, and it could be

because it is produced in a farther away region. Magnification in the red wing of the $H\alpha$ broad emission line has been detected in HE0435-1223 (Braibant et al. 2014) and QSO2237+0305 (Braibant et al. 2016). The main conclusion is that these line profile distortions are explained by the differential magnification of a Keplerian disk model. As the continuum region is expected to be smaller than the BLR, those profile distortions are also accompanied by larger magnification of the continuum. However, in our case the magnification in the continuum is smaller than the one in the $H\alpha$ broad emission line. On the other hand, several papers describe an enhancement in the Fe $K\alpha$ profile with higher magnification than the X-ray continuum in MG J0414+0534 (Chartas et al. 2002), QSO 2237+0305 (Dai et al. 2003) and H1413+117 (Chartas et al. 2004). This effect is attributed to differential microlensing. Popović et al. 2003 use a standard accretion disk and caustic crossing to investigate the structure that could lead to such differences. The authors conclude that different dimensions for the emitting region (e.g. an inner BEL anuli radius smaller than the continuum disk) and ‘segregation of emitters allow us to reproduce the Fe $K\alpha$ enhancement without equivalent continuum amplification’. Furthermore, Abajas et al. 2007 demonstrated that this result could also be obtained in the case of a biconic model for the BEL. Thus, a similar effect might be used to explain our results, but a further analysis is needed to confirm this.

The FWHM was measured for the three emission lines and are in agreement for $H\beta$ and $MgII$ for both images. Even though $H\alpha$ has a discrepancy in the right wing, we measured the FWHM for both of them (with a difference of > 5 sigma).

Microlensing effect in the continuum was investigated obtaining the magnitude difference for the continuum ($0.01 \pm 0.03 \text{ mag}$) and the core of the emission lines ($0.17 \pm 0.05 \text{ mag}$). Our values are in agreement with spectroscopic data from Nierenberg et al. 2020 and with photometric data corrected by time-delay. There seems to be microlensing effect in the continuum of $\Delta m = -0.16 \pm 0.06 \text{ mag}$.

The monochromatic luminosity at 5100 \AA was obtained for $H\alpha$ and $H\beta$ using a single-power law function to the region of interest. The luminosities for both images are in good agreement, with a mean of $\log_{10}(L_{5100}/L_{\odot}) = 44.29 \pm 0.20$. On the other hand, L_{3000} was estimated using SED and obtained $\log_{10}(L_{3000}/L_{\odot}) = 44.23 \pm 0.19$. Both luminosities are in agreement within errors.

The M_{BH} was measured with the luminosity and the FWHM from the broad emission lines, obtaining a consistent mass for both images in the same BEL and a mean mass of $\log_{10}(M_{BH}/M_{\odot}) = 8.37 \pm 0.40$ for this quadruple lensed quasar. When combined with the quasar’s monochromatic luminosities, we find Eddington ratios similar to those measured in the literature for unlensed low-luminosity quasars. Finally, we got the accretion disk size from equation 5 obtaining an average size of $\log_{10}(r_s/\text{cm}) = 15.28 \pm 0.63$.

Acknowledgements. A.M. acknowledges grant support from project CONICYT-PFCHA/Doctorado Nacional/2017 folio 21171499. V.M. acknowledges partial support from Centro de Astrofísica de Valparaíso. V.M. acknowledges support from Redes #190147 (ANID). N. G. acknowledges financial support from ICM Núcleo Milenio de Formación Planetaria, NPF. N. G. acknowledges grant support from project CONICYT-PFCHA/Doctorado Nacional/2017 folio 21170650. R.J.A. was supported by FONDECYT grant number 1191124.

References

Abajas, C., Mediavilla, E., Muñoz, J. A., Gómez-Álvarez, P., & Gil-Merino, R.

Table 2. FWHM, luminosities and M_{BH} .

Image	Line	FWHM [km/s]	$\log_{10}(L_{ref})[L_{\odot}]^a$	$\log_{10}(M_{BH}) [M_{\odot}]$	$\log_{10}(r_s) [cm]^b$	S/N Line ^c	S/N Continuum
A	MgII	3914.52 ± 500.09	44.23 ± 0.19	8.25 ± 0.59	14.92 ± 0.31	30	5
	H β	4689.32 ± 42.96	44.29 ± 0.17	8.27 ± 0.24	15.26 ± 0.79	16	6
	H α	5595.68 ± 125.92	44.36 ± 0.23	8.57 ± 0.22	15.63 ± 0.83	73	11
B	MgII	4118.73 ± 921.90	44.23 ± 0.19	8.29 ± 0.88	14.95 ± 0.23	35	6
	H β	4817.63 ± 48.15	44.21 ± 0.16	8.24 ± 0.21	15.23 ± 0.85	19	6
	H α	6150.98 ± 133.39	44.29 ± 0.23	8.61 ± 0.27	15.66 ± 0.74	85	12

Notes. ^(a) L_{ref} = Luminosity (L_{3000} , L_{5100} , L_{5100}) for MgII, H α and H β respectively. The luminosity for H α and H β is from the spectra and for MgII is obtained from the SED. ^(b) r_s is the accretion disk size obtained from equation 5 at the λ_{rest} of the emission line used for the M_{BH} measurement. ^(c) This is the maximum S/N in the peak of the emission line.

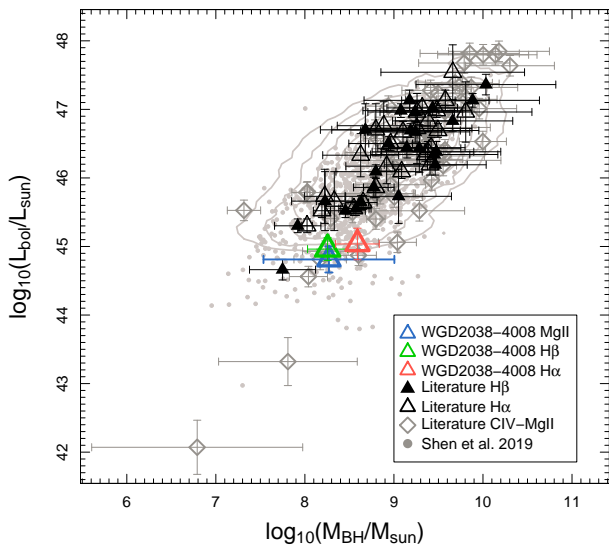


Fig. 9. M_{BH} vs L_{bol} for quasars. The masses plotted are estimated from different emission lines and monochromatic luminosity that exists upto date (Peng et al. 2006; Assef et al. 2011; Sluse et al. 2012; Ding et al. 2017). For lensed quasars, black open diamonds correspond to the M_{BH} derived from MgII and CIV emission line, black triangle correspond to H α and black filled triangle to H β emission line. For non-lensed quasars, we included data from Shen et al. 2019 for M_{BH} from SDSS represented by the grey dots and grey contours. The average M_{BH} mass estimation for WGD2038-4008 is represented as blue/red/green triangles for MgII/Hbeta/Halpha emission lines.

2007, ApJ, 658, 748

Abajas, C., Mediavilla, E., Muñoz, J. A., Popović, L. Č., & Oscoz, A. 2002, ApJ, 576, 640

Agnello, A., Lin, H., Kuropatkin, N., et al. 2018, MNRAS, 479, 4345

Anguita, T., Schmidt, R. W., Turner, E. L., et al. 2008, A&A, 480, 327

Assef, R. J., Denney, K. D., Kochanek, C. S., et al. 2011, ApJ, 742, 93

Assef, R. J., Kochanek, C. S., Brodwin, M., et al. 2010, ApJ, 713, 970

Bentz, M. C., Peterson, B. M., Netzer, H., Pogge, R. W., & Vestergaard, M. 2009, ApJ, 697, 160

Blandford, R. D. & McKee, C. F. 1982, ApJ, 255, 419

Bonvin, V., Courbin, F., Suyu, S. H., et al. 2017, MNRAS, 465, 4914

Braibant, L., Hutsemékers, D., Sluse, D., & Anguita, T. 2016, A&A, 592, A23

Braibant, L., Hutsemékers, D., Sluse, D., Anguita, T., & García-Vergara, C. J. 2014, A&A, 565, L11

Buckley-Geer, E. J., Lin, H., Rusu, C. E., et al. 2020, MNRAS[arXiv:2003.12117]

Bujarrabal, V., Guibert, J., & Balkowski, C. 1981, A&A, 104, 1

Cappellari, M. 2017, MNRAS, 466, 798

Cappellari, M. & Emsellem, E. 2004, PASP, 116, 138

Chang, K. & Refsdal, S. 1979, Nature, 282, 561

Chartas, G., Agol, E., Eracleous, M., et al. 2002, ApJ, 568, 509

Chartas, G., Eracleous, M., Agol, E., & Gallagher, S. C. 2004, ApJ, 606, 78

Courbin, F., Chantry, V., Revaz, Y., et al. 2011, A&A, 536, A53

Dai, X., Chartas, G., Agol, E., Bautz, M. W., & Garmire, G. P. 2003, ApJ, 589, 100

Dai, X., Kochanek, C. S., Chartas, G., et al. 2010, ApJ, 709, 278

Dark Energy Survey Collaboration, Abbott, T., Abdalla, F. B., et al. 2016, MNRAS, 460, 1270

Deeming, T. J. 1964, MNRAS, 127, 493

Ding, X., Treu, T., Suyu, S. H., et al. 2017, MNRAS, 472, 90

Eigenbrod, A., Courbin, F., Vuissoz, C., et al. 2005, A&A, 436, 25

Falco, E. E., Impey, C. D., Kochanek, C. S., et al. 1999, ApJ, 523, 617

Ferrarese, L. & Ford, H. 2005, Space Sci. Rev., 116, 523

Ferrarese, L. & Merritt, D. 2000, ApJ, 539, L9

Fian, C., Guerras, E., Mediavilla, E., et al. 2018, ApJ, 859, 50

Francis, P. J. & Wills, B. J. 1999, in Astronomical Society of the Pacific Conference Series, Vol. 162, Quasars and Cosmology, ed. G. Ferland & J. Baldwin, 363

Freudling, W., Romaniello, M., Bramich, D. M., et al. 2013, A&A, 559, A96

Gaia Collaboration, Prusti, T., de Bruijne, J. H. J., et al. 2016, A&A, 595, A1

Glikman, E., Helfand, D. J., & White, R. L. 2006, ApJ, 640, 579

Goad, M. R., Korista, K. T., & Ruff, A. J. 2012, MNRAS, 426, 3086

Greene, J. E., Peng, C. Y., & Ludwig, R. R. 2010, ApJ, 709, 937

Guerras, E., Mediavilla, E., Jimenez-Vicente, J., et al. 2013, ApJ, 764, 160

Hogg, D. W. 1999, arXiv e-prints, astro

Jiménez-Vicente, J., Mediavilla, E., Kochanek, C. S., et al. 2014, ApJ, 783, 47

Kaspi, S., Maoz, D., Netzer, H., et al. 2005, ApJ, 629, 61

Kaspi, S., Smith, P. S., Netzer, H., et al. 2000, ApJ, 533, 631

Kausch, W., Noll, S., Smette, A., et al. 2015, A&A, 576, A78

Kormendy, J. & Ho, L. C. 2013, ARA&A, 51, 511

Krone-Martins, A., Graham, M. J., Stern, D., et al. 2019, arXiv e-prints, arXiv:1912.08977

Lee, C.-H. 2019, PASA, 36, e011

Lemon, C., Auger, M. W., McMahon, R., et al. 2020, MNRAS, 494, 3491

Marconi, A. & Hunt, L. K. 2003, ApJ, 589, L21

McLure, R. J. & Dunlop, J. S. 2004, MNRAS, 352, 1390

Mediavilla, E., Jiménez-Vicente, J., Fian, C., et al. 2018, ApJ, 862, 104

Mediavilla, E., Muñoz, J. A., Falco, E., et al. 2009, ApJ, 706, 1451

Mediavilla, E., Muñoz, J. A., Kochanek, C. S., et al. 2005, ApJ, 619, 749

Mediavilla, E., Muñoz, J. A., Kochanek, C. S., et al. 2011, ApJ, 730, 16

Mejía-Restrepo, J. E., Trakhtenbrot, B., Lira, P., Netzer, H., & Capellupo, D. M. 2016, MNRAS, 460, 187

Morgan, C. W., Hyer, G. E., Bonvin, V., et al. 2018, ApJ, 869, 106

Morgan, C. W., Kochanek, C. S., Morgan, N. D., & Falco, E. E. 2010, ApJ, 712, 1129

Mosquera, A. M. & Kochanek, C. S. 2011, ApJ, 738, 96

Motta, V., Mediavilla, E., Falco, E., & Muñoz, J. A. 2012, ApJ, 755, 82

Motta, V., Mediavilla, E., Muñoz, J. A., et al. 2002, ApJ, 574, 719

Motta, V., Mediavilla, E., Rojas, K., et al. 2017, ApJ, 835, 132

Moustakas, L. A. & Metcalf, R. B. 2003, MNRAS, 339, 607

Narayan, R. & Bartelmann, M. 1996, arXiv e-prints, astro

Nierenberg, A. M., Gilman, D., Treu, T., et al. 2020, MNRAS, 492, 5314

Peng, C. Y., Impey, C. D., Rix, H.-W., et al. 2006, ApJ, 649, 616

Peterson, B. M. 1993, PASP, 105, 247

Peterson, B. M., Ferrarese, L., Gilbert, K. M., et al. 2004, ApJ, 613, 682

Poindexter, S., Morgan, N., & Kochanek, C. S. 2008, ApJ, 673, 34

Pooley, D., Blackburne, J. A., Rappaport, S., & Schechter, P. L. 2007, ApJ, 661, 19

Popović, L. Č., Mediavilla, E. G., Jovanović, P., & Muñoz, J. A. 2003, A&A, 398, 975

Rojas, K., Motta, V., Mediavilla, E., et al. 2020, ApJ, 890, 3

Schulze, A. & Wisotzki, L. 2010, A&A, 516, A87

- Shajib, A. J., Birrer, S., Treu, T., et al. 2019, *MNRAS*, 483, 5649
- Shakura, N. I. & Sunyaev, R. A. 1973, *A&A*, 500, 33
- Shang, Z., Wills, B. J., Wills, D., & Brotherton, M. S. 2007, *AJ*, 134, 294
- Shen, Y., Greene, J. E., Strauss, M. A., Richards, G. T., & Schneider, D. P. 2008, *ApJ*, 680, 169
- Shen, Y., Grier, C. J., Horne, K., et al. 2019, *ApJ*, 883, L14
- Shen, Y. & Liu, X. 2012, *ApJ*, 753, 125
- Shen, Y., Richards, G. T., Strauss, M. A., et al. 2011, *ApJS*, 194, 45
- Sluse, D., Hutsemékers, D., Courbin, F., Meylan, G., & Wambsganss, J. 2012, *A&A*, 544, A62
- Sluse, D. & Tewes, M. 2014, *A&A*, 571, A60
- Smette, A., Sana, H., Noll, S., et al. 2015, *A&A*, 576, A77
- Trakhtenbrot, B. & Netzer, H. 2012, *MNRAS*, 427, 3081
- Tremaine, S., Gebhardt, K., Bender, R., et al. 2002, *ApJ*, 574, 740
- Treu, T. 2010, *ARA&A*, 48, 87
- Treyer, M. & Wambsganss, J. 2004, *A&A*, 416, 19
- Vanden Berk, D. E., Richards, G. T., Bauer, A., et al. 2001, *AJ*, 122, 549
- Vanden Berk, D. E., Wilhite, B. C., Kron, R. G., et al. 2004, *ApJ*, 601, 692
- Vazdekis, A., Sánchez-Blázquez, P., Falcón-Barroso, J., et al. 2010, *MNRAS*, 404, 1639
- Vernet, J., Dekker, H., D'Odorico, S., et al. 2011, *A&A*, 536, A105
- Vestergaard, M. 2004, *ApJ*, 601, 676
- Vestergaard, M. & Osmer, P. S. 2009, *ApJ*, 699, 800
- Vestergaard, M. & Peterson, B. M. 2006, *ApJ*, 641, 689
- Wambsganss, J. 2006, in *Saas-Fee Advanced Course 33: Gravitational Lensing: Strong, Weak and Micro*, ed. G. Meylan, P. Jetzer, P. North, P. Schneider, C. S. Kochanek, & J. Wambsganss, 453–540
- Wright, E. L., Eisenhardt, P. R. M., Mainzer, A. K., et al. 2010, *AJ*, 140, 1868
- Yonehara, A., Hirashita, H., & Richter, P. 2008, *A&A*, 478, 95